Impact of Charge Carrier Injection/Extraction Performances in Low-Dimension PEDOT:PSS Organic Electrochemical Transistors

Galyna Sych, Patrice Rannou, Maxime Jullien-Palletier, Saïd Sadki, Yvan Bonnassieux, Sébastien Sanaur

ADVANCED ELECTRONIC MATERIALS
Open Access
www.advelectronicmat.de

Impact of Charge Carrier Injection/Extraction Performances in Low-Dimension PEDOT:PSS Organic Electrochemical Transistors

*Galyna Sych, Patrice Rannou, Maxime Jullien-Palletier, Saïd Sadki, Yvan Bonnassieux, and Sébastien Sanaur**

Organic electrochemical transistors (OECT) are gaining momentum in future applications of biosensors and bioelectronics. Nonetheless, contact (or series) resistances ($R_{S/D}$) remain underexplored, even though physical processes between the source/drain electrodes and organic mixed ionic-electron conductors (OMIECs) drive a substantial part of their performances. To address this shortcoming, in this study, low-dimension OECTs featuring 2 µm-long poly(3,4-ethylenedioxythiophene) and polystyrene sulfonate acid (PEDOT:PSS) channel are explored. Normalized contact resistances ($R_{S/D} \cdot W$) values as low as 1.4 Ω cm are obtained. It is observed that channel PEDOT:PSS thickness is not detrimental to $R_{S/D}$ but is impacting the cut-off frequency. A figure-of-merit (h) expressing the charge-carrier injection (or extraction, respectively) efficiency shows that planar depletion-mode OECTs are not contact-limited up to $L = 30$ µm channel length. Finally, an unprecedented approach that highlight the importance of optimizing the microfabrication technologies is shown, by decreasing the contact overlap length, according to OMIECs physicochemical contact properties. Indeed, a transfer-length method coupled to a current-crowding model allow to fully understand the behavior of low-dimension PEDOT:PSS OECTs and next, to optimize its circuits design. This is paving the way toward the development of OECTs-based integrated circuits with faster switching speed, broadening further their scopes and future use as advanced bioelectronics platforms.

1. Introduction

Organic electrochemical transistors (OECTs) are gaining momentum as next generation biosensors.[1–6] The first three gold electrode-based OECT device was first demonstrated by White et al. in 1984, using conducting polypyrrole as its active layer.[7] Intensive research efforts invested into physical modeling were instrumental to understand and master both the steady-state and transient responses of OECTs.[8] Replacing conducting polypyrrole with a third generation conducting polymers such as poly(3,4-ethylenedioxythiophene) doped with polystyrene sulfonate (PEDOT:PSS) allowed extraction of figures-of-merit (FoMs) values competing with current state-of-the-art electrolyte-gated transistors, especially for g_m transconductance $\left[g_m = \left(\frac{\partial I_{DS}}{\partial V_{GS}} \right)_{V_{DS,linear}} \right]$ value.[9] In PEDOT:PSS based-OECT, a positive biased Gate voltage (V_{GS}) drags negative ions out of the full volume of a gating electrolyte. Oppositely, countered

G. Sych, P. Rannou
Univ. Grenoble Alpes
Univ. Savoie Mont Blanc
CNRS
Grenoble INP
LEPMI
Grenoble 38000, France

The ORCID identification number(s) for the author(s) of this article can be found under https://doi.org/10.1002/aelm.202201067.

DOI: 10.1002/aelm.202201067

M. Jullien-Palletier, S. Sanaur
Mines Saint-Etienne
Centre Microelectronique de Provence
Department of Flexible Electronics
Gardanne F-13541, France
E-mail: sanaur@emse.fr

S. Sadki
Univ. Grenoble Alpes
CNRS
CEA
INAC-SyMMES
Grenoble 38000, France

Y. Bonnassieux
Laboratoire de Physique des Interfaces et des Couches Minces (LPICM)
UMR7647 CNRS – École Polytechnique – Institut Polytechnique de Paris
Route de Saclay
Palaiseau Cedex 91128, France

ADVANCED ELECTRONIC MATERIALS
Open Access
www.advelectronicmat.de

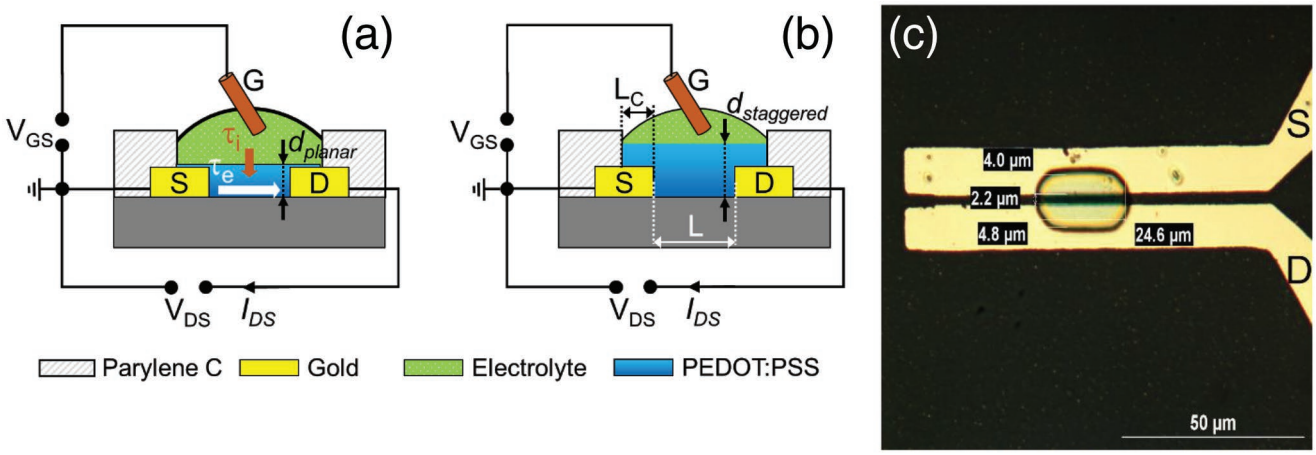

Figure 1. Bottom contact—Top Gate (BC-TG) OECT in a) staggered or b) planar architectures. c) Microphotograph of OECT with 45% and 55% channel overlap with S&D electrodes, respectively ($W \approx 25$ µm; $L = 2.2$ µm; $L_c^{fab} = 4$ and 4.8 µm, respectively). The scale bar is worth 50 µm.

positive ions enter into the bulk of PEDOT:PSS thin-film and pair up with fixed negative charges from PSS by electrostatic interactions. Consequently, the number of free charge carriers is decreasing onto the PEDOT backbone. Due to the application of a positive V_{GS} bias, the current between Source and Drain (I_{DS}) is consequently decreasing, leading to a so-called depletion mode PEDOT:PSS OECT. Electronic charge carriers within OECTs (i.e., polarons and bipolarons) are relatively mobile under the negative Source and Drain voltage (V_{DS}) bias applied. In a nutshell, OECT relies on ionic-to-electronic transduction in a three-terminal device configuration, exhibiting two-key parameters: i) the time for ions (τ_i) to enter into the bulk of the channel consisting of organic mixed ionic-electronic conductor (OMIEC) and ii) the time for electronic charge carriers (τ_e) to transit from Source to Drain (S&D) electrodes (**Figure 1**a,b). Ion permeability, swelling effect, channel thickness, volumetric capacitance dependencies of PEDOT:PSS have been extensively studied, discussed and commented in the literature to rationalize the observation of high FoM values.[10–13] Nonetheless, the underlying physics and electrochemistry of OECTs are not completely understood till date, some critical mechanisms remaining underexplored.[14] This is notoriously the case of the injection (or extraction) efficiency of electronic charge carriers localized at the interface between the PEDOT:PSS channel and the Source (or Drain, respectively) electrode. This is particularly surprising since an interfacial mechanism is driving the final performance of any transistor devices, particularly when it comes to reach bioelectronics logic circuits and neuromorphic applications.[15–17] A recent publication confirmed such importance by evaluating the influence of disorder on transfer characteristics of OECTs for which the contact resistance (R_S or R_D) amount compared to the total resistance of the device (R_{OECT}) was limiting the performances of OECTs featuring PEDOT:PSS as its OMIEC-based channel material.[18] From an analytical modeling approach, Lüssem et al. reported the effect of contact resistance on PEDOT:PSS OECTs with different doping level.[19] Even if addressed through a modeling approach, such limiting parameters have not been experimentally investigated till date in lower dimension channel OECT ($L < 50$ µm).[20,21] Nonetheless, this evaluation is critical to enable the advanced design of higher performance OECT electronic devices and the integration density of these building blocks into electronic circuitry without altering their intrinsic electronic performance.

In this work, we investigate these issues in low-dimension OECTs, varying the OECT's channel length (L) from 30 µm down to 2 µm with a <5 µm overlap contact length (L_C^{fab}) between the S&D electrodes and using PEDOT:PSS as the channel material. Normalized contact resistance values ($R_{S/D}$·W) as low as 1.4 Ω cm are obtained. For planar OECTs, it was found that PEDOT:PSS channel thickness is not detrimental to $R_{S/D}$ but is strongly affecting the cut-off frequency. PEDOT:PSS OECT dynamic response shows a total OECT switching time (τ_{OECT}) of 85 µs (i.e., ≈12 kHz) versus an electronic switching time (τ_e) of 2.8 µs (i.e., ≈357 kHz) that is contradictory with the measured cut-off frequency. This is confirming that ionic switching time (τ_i) is drastically limiting OECTs dynamic response. A charge-carrier injection (or extraction, respectively) efficiency FoM is showing that planar depletion-mode OECTs are not contact-limited up to $L = 30$ µm channel length. L_C is below the calculated characteristic contact length (L_T) for planar or staggered OECTs, implying that series resistances should be therefore considered as affected by technological micro-fabrication. Finally, considering that the length at the convergent point (L_{conv}) is acting as an "extension length" in the channel resistance, for $L < -L_{conv}$, the nature of the Source (or Drain)/OMIEC contact is definitively affecting the dynamic response of OECTs.

2. Results sand Discussion

2.1. Planar and Staggered OECTs

2.1.1. Device Architecture

Schematic representations of OECT in the so-called staggered and planar architecture are depicted in Figure 1a,b, respectively. A silver/ silver chloride (Ag/AgCl) electrode is here used as the Gate (G) electrode and immersed into an electrolytic medium

(e.g., consisting here in a liquid electrolyte). This electrolyte is in intimate contact with the PEDOT:PSS active layer and coated atop the S&D electrodes in the case of planar OECTs. The PEDOT:PSS channel material here is formulated to improve its bulk dc-conductivity up to 740 S cm^{-1} (see Experimental Section).

Planar (Figure 1a) versus staggered (Figure 1b) OECTs are simply defined and differentiated by varying the number of spin-coated PEDOT:PSS layers with an unchanged gold S&D electrodes thickness. We succeeded in tuning the PEDOT:PSS channel layer from one to three PEDOT:PSS spin-coated layers (see Experimental Section). The channel thickness of OECTs is evaluated through the extraction of capacitance values from a Electrochemical Impedance Spectroscopy (EIS) measurements setup, as previously reported.[22] Capacitances are extracted for all investigated channel areas ($W{\cdot}L$), in case of planar or staggered OECTs (Figure S1, Supporting Information). Fitted slopes in Figure S1 (Supporting Information) were found to be similar to the interfacial capacitance either capacitance per unit area (C_i in F cm^{-2}) or Double Layer capacitance (C_{DL}) that usually establish (O)FETs or EG(O)FETs FoMs.[23–28] Considering that the PEDOT:PSS capacitance per unit volume (C^*) is largely reported in the literature for the exact similar PEDOT:PSS formulation used here, we directly extract the OECTs thicknesses.[12,27] For $C^*_{PEDOT:PSS}$ = 39 F cm^{-3} and $C_i = C_{DL} = d{\cdot}C^*$, calculated thicknesses are $d_{planar} \approx 220$ nm and $d_{staggered} \approx 690$ nm, respectively. We notice that the ratio of slopes in Figure S1 (Supporting Information) for one or three spin-coated layers is 27/8.74 ≈ 3.09; a ratio that is in a very good agreement with the ratio of spin-coated layers. The gold S&D electrodes are 200 nm-thick in all OECT devices (see Experimental Section). Figure 1c shows an optical microphotograph of fabricated low-dimensional OECTs with channel length (L) down to ≈2 µm. S&D gold electrodes (200 nm-thick) are protected by a parylene C (transparent) layer, except in the opening filled by light blue-colored PEDOT:PSS layer (Figure 1c). The microfabrication step involving the second photomask alignment is the critical step to achieve low overlap contact lengths (L_C) between an OMIEC and S&D electrodes (Figure S2). Micro-fabricated OECTs used in this work show typically $L_C \approx 5$ µm overlap and channel lengths (L) varying from 32, 22, 11, 6, 3 µm (down to 2 µm) for 2 different channel widths (W = 25 µm or W = 50 µm) (2 columns of 2 × 5 OECTs) (Figure S3, Supporting Information).

2.1.2. Channel Thickness and Length Effects on Figures-of-Merits (FoMs)

Transconductance (in the Saturation Regime) and $\mu_{OECT}C^*$ Characteristics: **Figure 2**a shows typical output curve of a PEDOT:PSS OECT below 1 V, with negative, V_{DS}, and positive, V_{GS}, varying from 0 to +0.6 V.

A low V_{GS} is maximizing the current (I_{DS}) flowing between Source and Drain electrodes, whereas a large V_{GS} is decreasing I_{DS}, as expected for a depletion-mode OECT. For low V_{DS} (V_{DS} < −0.05 V), linear I_{DS} dependence was observed, highlighting no particular Series Resistances at Source and Drain electrode ($R_{S/D}$) effects. At higher V_{GS} and V_{DS}, I_{DS} is going first through a saturation effect but also toward a "negative" resistance (V_{GS} = 0.4; 0.5; 0.6 V) since I_{DS} is going below the saturation Drain current. From g_m transconductance, we extract $\mu_{OECT}C^*$ as:

$$\mu_{OECT}C^* = \frac{L}{Wd}\frac{g_m}{(V_{Th} - V_{GS})} \quad (1)$$

where W, L, and d are the channel width, length and thickness, respectively; μ is the charge-carrier mobility; C^* is the capacitance per unit volume of the channel; and V_{Th} is the threshold voltage. The $\mu_{OECT}C^*$ product is increasing according to the channel length (L) (Figure 2b), both in case of planar or staggered OECTs. Nonetheless, the $\mu_{OECT}C^*$ product is not rigorously linearly dependent in the case of planar OECTs. It is noteworthy that a $\mu_{OECT}C^*$ dispersion was already reported for PEDOT:PSS OECTs and is mitigating such a trend.[29] Moreover, the $\mu_{OECT}C^*$ product is reaching higher values in case of thinner planar channel OECTs (Figure 2b). Such dependencies on the geometrical thickness (d) and length (L) are theoretically expected from Equation (1). Figure 2b plots $\mu_{OECT}C^*$ values where g_m was considered to its maximal values. The V_{GS} to apply (in order to get a maximal g_m) ($V_{GS}^{g_{m,max}}$) is decreasing as long as L increases and seems to reach a plateau starting from $L \approx 20$ µm (Figure 2b). Moreover, $V_G^{g_{m,max}}$ is lowered in case of planar OECT (Figure 2b). Assuming that C^* is i) constant since the same formulation is used in all OECTs and ii) only a materials-dependent parameter, carrier mobility (μ_{OECT}) is hence varying according to the channel length (L)

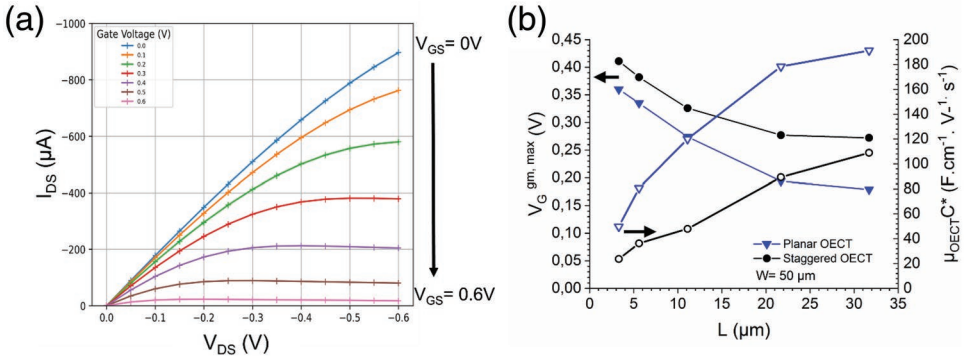

Figure 2. a) Typical output ($I_{DS} - V_{DS}$) curve for a planar PEDOT:PSS-based OECT (L = 11 µm, W = 50 µm). Gate voltages (V_{GS}) are biased from 0 V to +0.6 V. b) $\mu_{OECT}C^*$ product (right) and V_{GS} at $g_{m,\ max}$ (left) as a function of channel length (L) for planar or staggered OECTs.

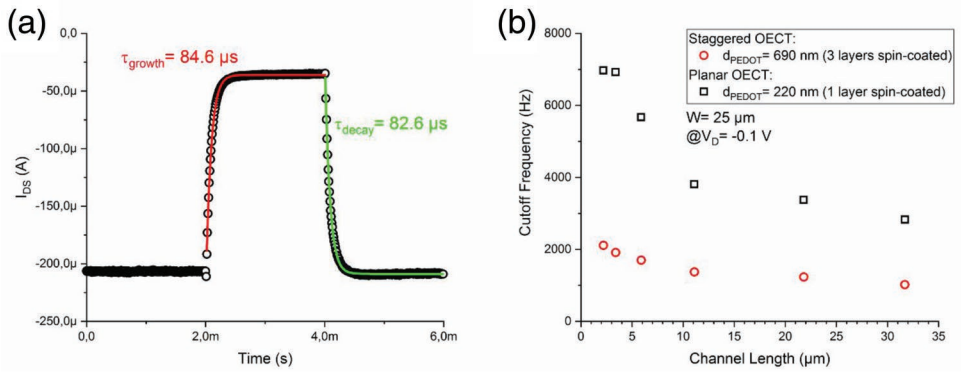

Figure 3. Drain current (I_{DS}) dynamic response according to a pulse Gate bias [ΔV_{GS} = 0.6 V, Δt = 2 ms]; L = 3 µm; W = 25 µm; V_{DS} = –0.4 V. a) Red and green lines represent fitted curves (exponential dependency) in forward and backward sweeps, respectively. b) Staggered or planar cut-off frequencies according to the channel length (L); W = 25 µm; V_{DS} = –0.1 V; V_{GS} = 0.6 V.

or thickness (d). From Figure 2b, one can observe that μ_{OECT} is ranging, according to the channel length, from 0.6 to 4.9 $cm^2\ V^{-1}\ s^{-1}$ (planar or staggered OECTs taken together). These values are in agreement with PEDOT:PSS OECTs reported values in the literature.[29,30] Such a device behavior implies that one has to take into account i) an effective charge carrier mobility, or similarly, contact resistances ($R_{S/D}$) effects or ii) disordered charge transport effects.

Dynamic Temporal Characteristics and Cut-Off Frequency: We investigated the dynamic response of OECTs according to a pulse square-wave with a ΔV_{GS} = 0.6 V amplitude during Δt = 2 ms time duration. **Figure 3**a represents I_{DS} dynamic response to the V_{GS} pulse. The tested OECT device shows a moderate hysteresis for a response time (τ_{OECT}) of 84.6 µs (i.e., f = 11.8 kHz) and 82.6 µs (i.e., f = 12.1 kHz) in forward and backward sweeps, respectively. Such a response time takes into account the total OECT response time (τ_{OECT}), involving the ions transit time (τ_i) and the electronic charge carrier transit time (τ_e), consequently (Figure 1a). Electronic charge carrier mobility (μ_{OECT}) was extracted from Equation (1) in order to calculate the electronic transit time (τ_e) following:

$$\tau_e = \frac{L^2}{\mu_{OECT} V_{DS}} \tag{2}$$

The τ_e values were found to be of ≈2.8 µs (i.e., f_c = 357 kHz) and ≈5.1 µs (i.e., f_c = 197 kHz) for planar and staggered OECTs, respectively (Figure S4, Supporting Information). OECT dynamic response is mainly limited by ions transit time (around $\tau_i \approx 80$ µs) as confirmed by direct measurements of OECT cut-off frequencies (f_c) (Figure 3b). One can notice importantly here that f_c is far from 357 kHz, when only electronic charge carriers are considered. Here like in previous results reported in the literature,[12,31,32] staggered OECTs have a slower response time in respect to planar OECTs. Figure 3b clearly shows higher cutoff frequencies in case of planar (or thinner) OECTs for each channel length. From those experimental results, we observe that the time for ions to deplete the PEDOT:PSS channel layer is lower in case of planar thinner OECTs. Indeed, it is not counter-intuitive to analyze that the cutoff frequency will be higher in case of thinner layer to deplete. It is then not surprising to observe cutoff frequencies damaged properties from thinner to thicker devices. This result also clearly states that the ions switching time is limiting OECTs performance. We notice a saturation effect at ≈7 kHz for L < 3 µm in case of planar OECTs. We point here that the cut-off frequencies' physical expression [f_c inversely proportional to the $L\cdot(L + L_C)$ product] do not satisfactorily fit the data displayed in Figure 3b.

Figure S5 (Supporting Information) shows the transfer characteristics for low V_{DS} = –0.1 V, at different channel lengths in case of planar PEDOT:PSS OECTs. From V_{GS} = +0.2 V to V_{GS} = +0.6 V, I_{DS} is increasing when the channel length is increasing, except for the lowest channel length, L = 2.2 µm. This trend is in accordance with Figure 3b results. Indeed, there is a cutoff frequency saturation at the similar lowest channel length, L = 2.2 µm. This is indicating a velocity saturation of charge carriers and thus a short-channel effect around L = 2 µm in planar PEDOT:PSS OECT. Nonetheless, such a statement is not taking into account overlapping effects of the PEDOT:PSS channel layer on the Source and Drain electrodes (Figure 1c).

2.2. Contact Resistances ($R_{S/D}$) and Characteristic Injection Length (L_T)

2.2.1. Contact Resistances ($R_{S/D}$)

The Transfer-Length Method (TLM) was used to calculate the contact (or series) resistances that arise at the interface between the Source (or Drain) electrode and the OMIEC (PEDOT:PSS) channel. It is a widespread method that is regularly used in (O)TFTs.[33–40] TLM is using a series of OECTs with different channel lengths measured at low source-drain voltage (**Figure 4**a). TLM is not destructive and does not disrupt the OMIEC thin-film morphology, since values are calculated exclusively using an analytical analysis. The total OECT resistance is (inset of Figure 4a):

$$R_{OECT} = \left(\frac{\partial V_{DS}}{\partial I_{DS}}\right)_{V_{DS}\to 0} = R_S + R_{ch} + R_D = 2R_{S/D} + \frac{L}{W\mu_i dC^*\left(V_{Th,i} - V_{GS}\right)} \tag{3}$$

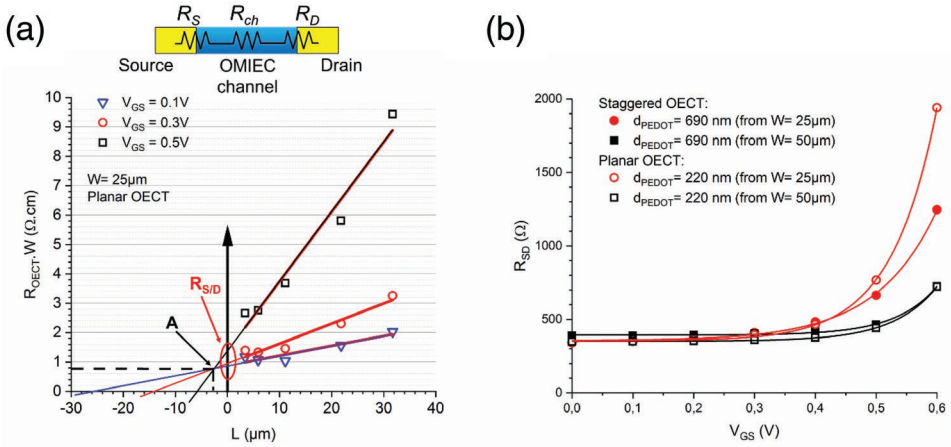

Figure 4. a) Transfer-Length Method (TLM) in the case of planar OECTs (Contact resistance $R_{S/D}$ at $L = 0$ µm and $A = [-L_{conv} = 2.6$ µm; $R_{conv} \times W = 0.8$ Ω cm] as convergent point). Contact resistance ($R_{S/D}$) according the Gate voltage (V_{GS}) [at $V_{DS} = -0.1$ V]. b) The dependency of the contact resistance is fitted by an exponential dependency, as $R_{S/D} = A \times \exp(B \times V_{GS}) + C$ (A, B, C constant parameters are regrouped in Table S1, Supporting Information).

where $R_{S/D}$ is the contact (or series) resistance; R_{ch} is the channel resistance; μ_i and $V_{Th,i}$ are the intrinsic mobility and threshold voltage, which represent conductive channel material, without the influence of series resistances. By plotting normalized total resistance R_{OECT}.W according to the channel length (L) and after extrapolating the experimental data with linear curves, the y-intercept (i.e., $L = 0$) reveals the total series resistances ($R_S + R_D$) while the slope gives the channel resistance per unit length (i.e., $r_{ch} = \frac{R_{ch}}{W}$) which is representative to the conduction channel material. Figure 4a shows normalized contact resistance ($R_{S/D} \cdot W$) values as low as 1 Ω cm for $V_{GS} = 0.3$ V, closely corresponding to V_{GS} where g_m is maximized. Over the OECT ON-resistance (i.e., $V_{GS} = 0.5$ V) to the OECT OFF-resistance (i.e., $V_{GS} = 0.1$ V) regimes, $R_{S/D} \cdot W$ is not exceeding 1.4 Ω cm. Such contact (or access) resistances ($R_{S/D}$) are remarkably low, particularly compared to OFETs. Indeed, in depletion mode, PEDOT:PSS OECT switches from ON-state to OFF-state for applied positive Gate voltage (from $V_{GS} = 0$ V to $V_{GS} = +0.6$ V) (Figure 2a). For low Gate voltage, the impedance mismatch between the metal gold electrode and the channel layer will be low, since the PEDOT:PSS channel layer is in a highly doped state (i.e., conducting). Moreover, gold work function is aligned with PEDOT:PSS HOMO level, making "ohmic" contact. This explains why contact resistances are low; particularly when compared to OFETs. Moreover, it is stated that PEDOT :PSS (or CPs) is showing low interface dipole, induced by contacts doping effect.[38,41–43] Moreover, the work function of pristine PEDOT is lower than that of gold, giving rise to an interface potential difference and heavy doping at low voltage. The charging of the PEDOT:PSS interface creates an Electrical-Double Layer.[44] At the opposite, "intrinsic" (non-doped) organic semiconductors (OSCs) (small molecules or polymers)/Metal interfaces show higher contact resistance, because of a more pronounced interface dipole existence. Charges injection on OSC or CPs/Metal contacts are modeled between Mott–Schottky and Bardeen interfaces. It is commonly adopted that organic electronics devices rely on both models.

L_{conv} is regarded as an equivalent extension of channel resistance.[45] Staggered or Planar OECTs show contact resistance ($R_{S/D}$) dependency to V_{GS} until 0.3 V (Figure 4b). Below such a V_{GS} value, the resistance to the injection (or to the extraction) of charge carriers is similar for staggered or planar OECT. This potentially contradicting result at first sight can in fact be reconciled by considering that PEDOT:PSS OECTs are operating in depletion-mode. Indeed, at low depletion state (i.e., low + V_{GS}), PEDOT:PSS OECT is highly doped. The PEDOT:PSS HOMO energetic level and the Au (Source/Drain) work function energetic level are aligned (around 5.0–5.2 eV): there is no energy barrier to the current flowing, almost making "Ohmic" contact. I_{DS} current is flowing through the interface (i.e., the contact) without "resistance": $R_{S/D}$ is thus low. Thin (low exchanged-surface with the contact) or thick (high exchanged-surface with the contact) channel PEDOT:PSS layer is not limiting the contact injection (extraction, respectively) efficiency because the channel layer is in a highly doped Level. At high depletion state, (i.e., high + V_{GS}), PEDOT:PSS channel layer is depleted with a low doping level (i.e., there are almost no free charge carriers). The number of charge carriers injected into the PEDOT:PSS becomes greater than that present at equilibrium (i.e., depleted case). The excess charge then forms a space-charge zone, creating an electric field opposing the injection of the carriers. PEDOT:PSS is observing a Space-Charge Limited Current (SCLC) effect. A screening effect is occurring at the Metal-conducting polymer interface (i.e., contact). The charge carrier injection (or extraction, respectively) efficiency is lowered, $R_{S/D}$ are thus increasing. In such a de-doped state, higher is the exchanged surface between the Metal and the conducting polymers, higher is the contact-limited effect. This means that $R_{S/D}$ will increase more according to V_{GS} (i.e., de-dedoped state) for staggered "thick" OECTs. Experimental data in Figure 4b were fitted according to the model developed by Kaphle et al. where the dependency of the contact resistance can be fitted by an exponential dependency, as: $R_{S/D} = A \times \exp(B \times V_{GS}) + C$.[19] Fitted parameters for staggered or planar PEDOT:PSS OECTs are regrouped in Table S1 (Supporting Information). Gate voltage is a depletion voltage and contact resistances grow exponentially according the Gate Voltage. Indeed, Figure 1a shows the OFF-state of the PEDOT:PSS OECT as the Gate voltage

Table 1. Contact ($R_{S/D}$) and channel (R_{ch}) resistances comparison as FoMs for OECT charge-carrier injection (or extraction) efficiency (η) at V_{GS} = 0.3 V and V_{DS} = −0.1 V.

OMIEC thickness [nm]	W [µm]	$R_{S/D}$ [Ω] (at V_{GS} = 0 V)	R_{ch} [Ω][a)]	η (%) for $L \to \infty$
690[b)]	25	356 ± 8	474 ± 138	48
690[b)]	50	393 ± 3	600 ± 200	42
220[c)]	25	353 ± 5	614 ± 148	56
220[c)]	50	351 ± 1	737 ± 148	60

[a)]For $V_{GS} \to 0$ (fitted from the empirical model expressed in Figure 4b); [b)]Staggered OECTs; [c)]Planar OECTs.

increases. In such an exponential growth dependency, the growth rate is similar for staggered or planar OECTs, between 10 and 15 units per volts (V^{-1}). That means the Gate voltage depletion effect is similar in any OECTs case. Contact resistances are more increasing in case of shorter channel width (W). Indeed, as the fitting equation is showing, the multiplication factor (A) is very different in case of the channel width (W = 25 µm or W = 50 µm). More especially, it is one order of magnitude larger for W = 25 µm channel width. Staggered and planar OECTs have similar PEDOT:PSS formulation, thus similar bulk conductivity and show thus similar contact resistance at V_{GS} = 0 V [$R_{S/D}$ (for V_{GS} = 0 V) = $A + C$ value]. **Table 1** summarizes the channel and series resistances values for the different case of OECTs, as well as a FoM, the charge-carrier injection efficiency (η) at the source electrode (or the extraction efficiency at the drain electrode, symmetrically):[38,46]

$$\eta = \frac{R_{ch}}{R_{S/D} + R_{ch}} \tag{4}$$

η is decreasing according to the channel length (Figure S6, Supporting Information), since R_{ch} is highly increasing according to the channel length. Interestingly, the channel resistance is always dominating the OECT behavior, meaning that PEDOT:PSS OECTs cannot be contact-limited for L < 20 µm. Such a physical meaning is of high interest for establishing geometrical design rules and envisioning OECT-based circuitry for (bio)electronic applications. By fitting such experimental data with exponential decay curves, we extrapolate this analysis to long channel lengths ($L \to \infty$). As can be seen in Figure S6 (Supporting Information) where the resistance to charge carrier injection (or extraction) is dominating over the OECT total resistance for L > 30 µm, this trend is not holding true for staggered OECTs (Table 1).

2.2.2. Characteristic Injection (or Extraction) Length (L_T)

The (O)TFT series resistances are closely related to the overlap between source (or drain) contact and gate contact (L_C). In case of BC-TG OECTs, L_C is determined by the Parylene C patterning that is insulating the electrolyte from the gold interconnections and source or drain contacts, thus patterning the OMIEC channel and overlap length (Figure 1b). In TFTs, the drain current does not usually flow through the whole source or drain contact but is limited to a specific area of contact or is efficiently injected (or extracted) in a characteristic (effective) length (L_T), expressed as:[47]

$$L_T = \frac{R_{S/D}}{r_{ch} \coth\left(\frac{L_C}{L_T}\right)} \tag{5}$$

The characteristic injection (or extraction) length (L_T) increases with channel thickness, the bulk density of states and the *source-to-drain* contact resistances.[48] It is a critical parameter for designing (O)TFTs. Its discussion is addressed hereinafter for OECTs. It is considered that there is no L_T effect in case of planar OECTs since the OMIEC channel is not overlapping with the contact electrode (**Figure 5**a). Current-crowding model is thus to consider in case of staggered transistors. Above the

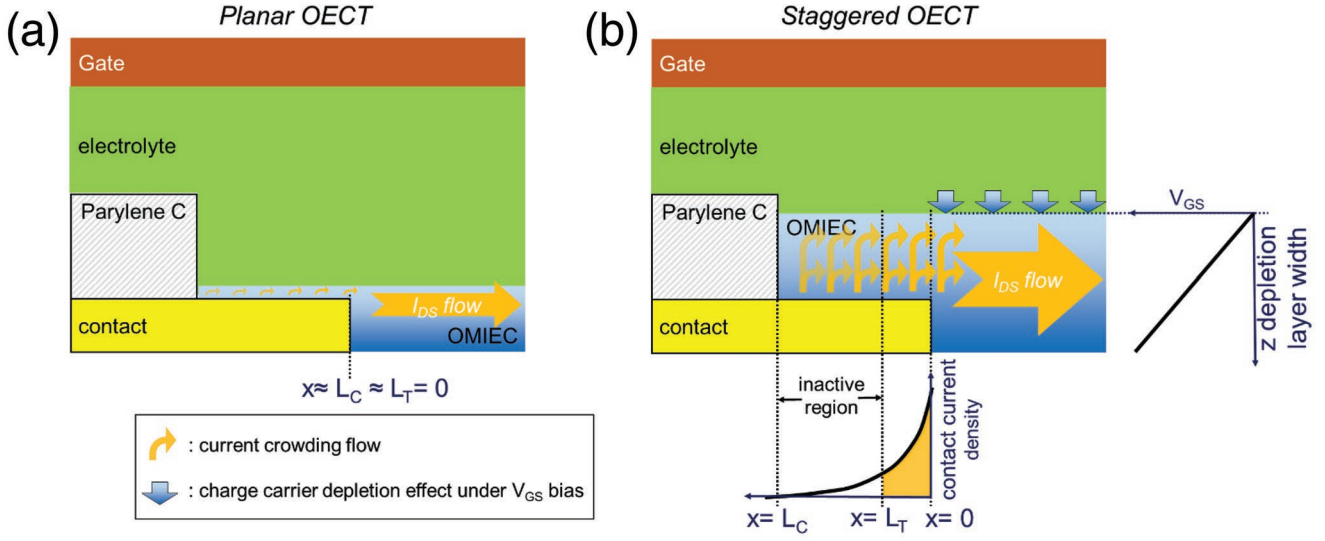

Figure 5. Current-crowding model in the schematics of charge injection mechanisms at the contact electrode/OMIEC interface, in a) planar or b) staggered OECTs.

L_T value, the contact dimension (L_C) has no influence on the parasitic contact (or series) resistances, since the current does not flow through the further part of the source or drain contact (inactive region) (Figure 5b). On the contrary, below L_T, the whole contact area is active with respect to the current flow: the resistance is roughly proportional to the reciprocal of the contact dimension (Equation (5)). Therefore, an increase in the contact dimension (L_C) does not affect the OECT contact (or series) resistance, but at the expense of enhancing parasitic *gate-to-source* or *gate-to-drain* capacitances. This is detrimental to increase the cut-off frequency of OECTs.[49,50]

The TLM method allows the extrapolation of $R_{S/D}$ and R_{ch} values (as expressed in Equation (3) and reported in Table 1) from linear curve fits. All converge on the same point (i.e., indicated as point *A* in Figure 4a). On this convergent point $A = [-L_{conv};\ R_{conv}]$, Equation (3) can be modified as:[45]

$$R_{S/D} = (-L_{conv})\frac{R_{ch}}{W} + R_{conv} \tag{6}$$

Equation (6) re-injected in Equation (5) leads to the approximated L_T expression:[31]

$$L_T \cong \begin{cases} L_{T1} = \dfrac{-L_{conv}}{2} + \dfrac{W}{2}\dfrac{R_{conv}}{R_{ch}}, \text{ when } L_{T1} \le \dfrac{L_C}{1.5} \\ L_{T2} = \sqrt{\left(L_{T1} - \dfrac{L_C}{3}\right)L_C}, \text{ when } L_{T1} > \dfrac{L_C}{1.5} \end{cases} \tag{7}$$

L_T is also calculated in the case of planar OECTs, since the PEDOT:PSS thickness (i.e., 220 nm-thick) is slightly higher than the gold contact electrodes (i.e., 200 nm-thick). This could be considered as the lowest contribution to current crowding effect we would validate, taking into consideration, as long as OECTs are fabricated by solution-process. L_C is below L_T for planar or staggered OECTs (**Figure 6**), meaning that series resistances should be therefore considered as affected by technological microfabrication issues. It should be logical then to increase

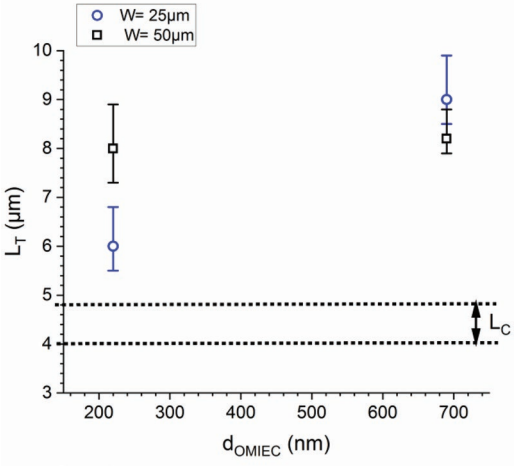

Figure 6. Characteristic injection length (L_T) for planar or staggered OECTs.

L_C to optimize the OECTs performances. This is without taking into account that cut-off frequency is decreasing with increasing L_C. Indeed, increasing L_C contributes to parasitic *gate-to-source* or *gate-to-drain* capacitances, corresponding to the inactive region, $\Delta L = L_C - L_T$ length difference, at the electrode/OMIEC interface (Figure 5). Nonetheless, it is not physically relevant here since $\Delta L < 0$. It does not explain thus the cut-off frequency saturation we observe in Figure 3b. Moreover, considering that L_{conv} is acting as an "extension length" in the channel resistance, for $L < -L_{conv} = 2.8$ µm, electrode/OMIEC contact is dominating the dynamic response of the OECT. Indeed, below $-L_{conv}$, cut-off frequency is starting to saturate for $L < 3$ µm, as observed in Figure 3b. Through an unprecedented approach, we experimentally prove here the importance to improve the OECTs micro-fabrication, as the layer-to-layer photolithography alignment, according to the electrode/OMIEC contact properties. We corroborate that the nature or the morphology of the interfacial layers, their doping states as well as the influence of defects or disorder in such OMIECs are of paramount importance in setting the overall OECTs performances.

3. Conclusion

We have designed and characterized depletion-mode OECTs with low-geometrical channel length ($L_{channel}$ = 2 µm) and overlap contact length (L_C = 5 µm) dimensions, showing normalized contact resistances ($R_{S/D}{\cdot}W$) values as low as 1.4 Ω cm, where the g_m transconductance is maximum. We observe that PEDOT:PSS channel thickness is not detrimental to $R_{S/D}$ but is affecting the cut-off frequency. PEDOT:PSS OECT dynamic response shows a total OECT switching time (τ_{OECT}) of 85 µs (i.e., ≈12 kHz) versus an electronic switching time (τ_e) of 2.8 µs (i.e., ≈357 kHz) that is contradictory with the measured cut-off frequency, saturating at 7 kHz. First, this confirms that the ionic switching time (τ_i) is drastically limiting OECTs dynamic response. Moreover, the figure-of-merit expressing a charge-carrier injection efficiency at the contact (or extraction, respectively) shows that depletion-mode planar OECTs are not contact-limited up to $L = 30$ µm channel length. Finally, we take here an unprecedented approach to highlight the importance to optimize the micro-fabrication technologies for manufacturing higher performance OECTs, by decreasing the overlap length between the electrodes and the OMIEC, according to the electrodes/OMIEC contact properties. Indeed, the application of the TLM coupled to a current-crowding model allowed us to better understand the behavior of low-dimension PEDOT:PSS OECTs and thus to optimize OECTs circuits design. We analyze that the overlap contact length (L_C) remains below the measured characteristic contact lengths (L_T) for planar or staggered OECTs, implying that series resistances should be therefore considered as affected by technological micro-fabrication. Finally, considering that L_{conv} is acting as an "extension length" in channel resistance, for $L < -L_{conv}$, the nature of the Source (or Drain)/OMIEC contact is definitively affecting the dynamic response of OECTs. Such an approach is paving the way toward the development of OECTs-based integrated circuits with faster switching speed, broadening further their scope and future uses as advanced bioelectronics platforms.

4. Experimental Section

Thin-Film OECTs Microfabrication: A 10 nm-thick chromium layer was deposited by Vacuum Thermal Evaporation (VTE) at a 10^{-6} Torr vacuum base pressure to 0.1 Å s^{-1} deposition rate. Consequently, 200 nm-thick gold layer was deposited by VTE (at a 10^{-6} Torr vacuum base pressure; 1.0 Å s^{-1} deposition rate), onto a 4 in. diameter glass wafer. AZ10XT (520 cps) photoresist (PR) was deposited by spin-coating for 35 s at 1750 rpm. An 8.9 µm-thick photoresist was exposed during 14 s at 20 mW cm^{-2} (@405 nm) through a chromium photomask with a Süss MicroTec MJB4 mask-aligner. The PR was baked at 110 °C for 120 s before to be developed with MF26A developer during 5 min. Consequently, Cr and Au layers were selectively etched in a hot NB Au etch 200 (Microchemicals) bath during 5 min at 60 °C. Finally, Cr layer was etched in a Technietch Cr01 bath. A first layer of 3 µm-thick Parylene C (PaC) was deposited (in a SCS coater), followed by the spin-coating of a Micro90 solution, and a second PaC layer (4 µm-thick) was deposited atop. Micro90 spin-coating decreased the adhesion between the 2 PaC layers. Photolithography and O_2 Reactive Ion Etching (200 W, 10 sccm CF_4, 50 sccm O_2, 50 min) was used to open the access to S&D gold electrodes. PEDOT:PSS was spin-coated for 30 s at 1500 rpm on such a patterned substrate. The second layer of PaC was removed by mechanical peeling, leaving the PEDOT:PSS only in the channel (Figure S1, Supporting Information). Parylene C film location was determining the overlap length (L_C) between Source (or Drain) electrode and the electrolyte + Gate electrode.

For the preparation of the PEDOT:PSS films, 20 mL of aqueous dispersion (PH-1000 from Heraeus Clevios GmbH), 5 mL of ethylene glycol, ≈50 µL of dodecyl benzene sulfonic acid were mixed and sonicated before spin-coating. The films were subsequently baked at 140 °C for 1 h onto a hot plate and immersed in deionized water to remove the excess of low molecular weight compounds: this was defined as the sequence (*A*) for one spin-coated layer. Three PEDOT:PSS spin-coated layers were deposited by repeating 3 times the A sequence. Four-probe measurements were given 270 Ω $\square^{-1}$. For a 50 nm thick-film, such a PEDOT:PSS formulation led to a bulk dc-conductivity value of ≈740 S cm^{-1}.

OECTs Electrochemical, Electrical, and Cut-Off Frequencies Measurements: Resistance along the gold interconnects was ≈40 Ω. This was considered as negligible in the data analysis since it only represented ≈10% the maximal measured $R_{S/D}$ resistance. These interconnects resistance level was similar for all devices investigated in this study; ruling out source of bias in the subsequently analyses performed. The PEDOT:PSS channel width, length, and overlap were measured through optical microscopy (Nikon) while the channel thickness was extracted with a mechanical profilometer (Dektak XT, Veeco). NaCl (100 mM) in deionized water was used as the liquid electrolytic medium, and a Ag/AgCl pellet as the gate electrode. A three-electrode configuration was used for the electrochemical impedance spectroscopy (EIS) measurements (Metrohm), with platinum and Ag/AgCl counter and reference electrodes, respectively. The source and drain electrodes were shorted together, and the channel was used as the working electrode. In OECTs, the wiring of the OECT is illustrated in Figure 1a, in a common source configuration, and tested using a National Instruments (NI) PXI system and custom LabView software. The drain bias was applied using a NI PXIe-4145 Source-Measure unit. A sinusoidal voltage signal was applied at the gate, with varying frequency and for amplitude of ΔV_{GS} = 10 mV. The drain current was measured using the NI PXI 4071 Digital Multimeter and was synchronized with the measured gate voltage using the built-in PXI architecture.

Supporting Information

Supporting Information is available from the Wiley Online Library or from the author.

Acknowledgements

The authors gratefully acknowledge the funding from the Agence Nationale de la Recherche (ANR) under the Grant ANR-20-CE06-022, supporting the collaborative research project MASTERMIND. This work was in part performed within the framework of the Centre of Excellence of Multifunctional Architectured Materials "CEMAM" under the ANR-10-LABX-44-01 Grant. G.S., P.R., and S.S. acknowledge supports from the Centre National de la Recherche Scientifique (CNRS) at the UMR5279-LEPMI and UMR5819-SyMMES labs and from the Université Grenoble Alpes at UMR5819-SyMMES labororatory, respectively.

Conflict of Interest

The authors declare no conflict of interest.

Data Availability Statement

The data that support the findings of this study are available from the corresponding author upon reasonable request.

Keywords

contact resistances, current crowding model, cutoff frequency, low dimensional OECTs, organic bioelectronics, planar and staggered OECTs

Received: September 20, 2022
Revised: December 1, 2022
Published online: January 3, 2023

[1] J. Rivnay, R. M. Owens, G. G. Malliaras, *Chem. Mater.* **2014**, *26*, 679.
[2] T. Someya, Z. Bao, G. G. Malliaras, *Nature* **2016**, *540*, 379.
[3] F. Torricelli, D. Z. Adrahtas, Z. Bao, M. Berggren, F. Biscarini, A. Bonfiglio, C. A. Bortolotti, C. D. Frisbie, E. Macchia, G. G. Malliaras, I. McCulloch, M. Moser, T.-Q. Nguyen, R. M. Owens, A. Salleo, A. Spanu, L. Torsi, *Nat. Rev. Methods Primers* **2021**, *1*, 66.
[4] B. D. Paulsen, S. Fabiano, J. Rivnay, *Annu. Rev. Mater. Res.* **2021**, *51*, 73.
[5] R. B. Rashid, X. Ji, J. Rivnay, *Biosens. Bioelectron.* **2021**, *190*, 113461.
[6] S. T. Keene, T. P. A. van der Pol, D. Zakhidov, C. H. L. Weijtens, R. A. J. Janssen, A. Salleo, Y. van de Burgt, *Adv. Mater.* **2020**, *32*, 2070148.
[7] H. S. White, G. P. Kittlesen, M. S. Wrighton, *J. Am. Chem. Soc.* **1984**, *106*, 5375.
[8] D. A. Bernards, G. G. Malliaras, *Adv. Funct. Mater.* **2007**, *17*, 3538.
[9] D. Khodagholy, J. Rivnay, M. Sessolo, M. Gurfinkel, P. Leleux, L. H. Jimison, E. Stavrinidou, T. Herve, S. Sanaur, R. M. Owens, G. G. Malliaras, *Nat. Commun.* **2013**, *4*, 2133.
[10] E. Stavrinidou, P. Leleux, H. Rajaona, D. Khodagholy, J. Rivnay, M. Lindau, S. Sanaur, G. G. Malliaras, *Adv. Mater.* **2013**, *25*, 4488.
[11] E. Stavrinidou, O. Winther-Jensen, B. S. Shekibi, V. Armel, J. Rivnay, E. Ismailova, S. Sanaur, G. G. Malliaras, B. Winther-Jensen, *Phys. Chem. Chem. Phys.* **2014**, *16*, 2275.
[12] J. Rivnay, P. Leleux, M. Ferro, M. Sessolo, A. Williamson, D. A. Koutsouras, D. Khodagholy, M. Ramuz, X. Strakosas, R. M. Owens, C. Benar, J.-M. Badier, C. Bernard, G. G. Malliaras, *Sci. Adv.* **2015**, *1*, e1400251.
[13] C. M. Proctor, J. Rivnay, G. G. Malliaras, *J. Polym. Sci., Part B: Polym. Phys.* **2016**, *54*, 1433.

[14] J. T. Friedlein, R. R. McLeod, J. Rivnay, *Org. Electron.* **2018**, *63*, 398.
[15] J. Rivnay, S. Inal, A. Salleo, R. M. Owens, M. Berggren, G. G. Malliaras, *Nat. Rev. Mater.* **2018**, *3*, 17086.
[16] D. Tu, S. Fabiano, *Appl. Phys. Lett.* **2020**, *117*, 080501.
[17] Q. Thiburce, N. A. Melosh, A. Salleo, *Flexible Printed Electron.* **2022**, *7*, 034001.
[18] J. T. Friedlein, J. Rivnay, D. H. Dunlap, I. McCulloch, S. E. Shaheen, R. R. McLeod, G. G. Malliaras, *Appl. Phys. Lett.* **2017**, *111*, 023301.
[19] V. Kaphle, S. Liu, A. Al-Shadeedi, C.-M. Keum, B. Lüssem, *Adv. Mater.* **2016**, *28*, 8766.
[20] P. R. Paudel, V. Kaphle, D. Dahal, R. K. Radha Krishnan, B. Lüssem, *Adv. Funct. Mater.* **2021**, *31*, 2004939.
[21] V. Kaphle, P. R. Paudel, D. Dahal, R. K. Radha Krishnan, B. Lüssem, *Nat. Commun.* **2020**, *11*, 2515.
[22] M. ElMahmoudy, A. M. Charrier, G. G. Malliaras, S. Sanaur, *Adv. Mater.* **2018**, *3*, 1700344.
[23] L. Herlogsson, Y.-Y. Noh, N. Zhao, X. Crispin, H. Sirringhaus, M. Berggren, *Adv. Mater.* **2008**, *20*, 4708.
[24] E. Said, O. Larsson, M. Berggren, X. Crispin, *Adv. Funct. Mater.* **2008**, *18*, 3529.
[25] L. Kergoat, L. Herlogsson, D. Braga, B. Piro, M. C. Pham, X. Crispin, M. Berggren, G. Horowitz, *Adv. Mater.* **2010**, *22*, 2565.
[26] D. Braga, M. Ha, W. Xie, C. D. Frisbie, *Appl. Phys. Lett.* **2010**, *97*, 193311.
[27] O. Larsson, A. Laiho, W. Schmickler, M. Berggren, X. Crispin, *Adv. Mater.* **2011**, *23*, 4764.
[28] L. Herlogsson, X. Crispin, S. Tierney, M. Berggren, *Adv. Mater.* **2011**, *23*, 4684.
[29] S. Inal, G. G. Malliaras, J. Rivnay, *Nat. Commun.* **2017**, *8*, 1767.
[30] M. ElMahmoudy, S. Inal, A. Charrier, I. Uguz, G. G. Malliaras, S. Sanaur, *Macromol. Mater. Eng.* **2017**, *302*, 1600497.
[31] A. G. Polyravas, N. Schaefer, V. F. Curto, A. B. Calia, A. Guimera-Brunet, J. A. Garrido, G. G. Malliaras, *Appl. Phys. Lett.* **2020**, *117*, 073302.
[32] P. R. Paudel, M. Skowrons, D. Dahal, R. K. Radha Krishnan, B. Lüssem, *Adv. Theory Simul.* **2022**, *5*, 2100563.
[33] K. Terada, H. Muta, *Jpn. J. Appl. Phys.* **1979**, *18*, 953.
[34] J. G. J. Chern, P. Chang, R. F. Motta, N. Godinho, *IEEE Electron Device Lett.* **1980**, *1*, 170.
[35] J. Kanicki, F. R. Libsch, J. Griffith, R. Polastre, *J. Appl. Phys.* **1991**, *69*, 2339.
[36] S. Luan, G. W. Neudeck, *J. Appl. Phys.* **1992**, *72*, 766.
[37] E. J. Meijer, G. H. Gelinck, E. van Veenendaal, B.-H. Huisman, D. M. de Leeuw, T. M. Klapwijk, *Appl. Phys. Lett.* **2003**, *82*, 4576.
[38] M. Barret, S. Sanaur, P. Collot, *Org. Electron.* **2008**, *9*, 1093.
[39] D. Boudinet, M. Benwadih, Y. Qi, S. Altazin, J.-M. Verilhac, M. Kroger, C. Serbutoviez, R. Gwoziecki, R. Coppard, G. L. Blevennec, A. Kahn, G. Horowitz, *Org. Electron.* **2010**, *11*, 227.
[40] C. Liu, Y. Xu, Y.-Y. Noh, *Mater. Today* **2015**, *18*, 79.
[41] A. Kahn, N. Koch, W. Gao, *J. Polym. Sci., Part B: Polym. Phys.* **2003**, *41*, 2529.
[42] J. Z. Wang, J. F. Chang, H. Sirringhaus, *Appl. Phys. Lett.* **2005**, *87*, 083503.
[43] M. Fahlman, S. Fabiano, V. Gueskine, D. Simon, M. Berggren, X. Crispin, *Nat. Rev. Mater.* **2019**, *4*, 627.
[44] K. Tybrandt, I. V. Zozoulenko, M. Berggren, *Sci. Adv.* **2017**, *3*, 3659.
[45] C. Liu, Y. Xu, G. Ghibaudo, X. Lu, T. Minari, Y.-Y. Noh, *Appl. Phys. Lett.* **2014**, *104*, 013301.
[46] Y. L. Shen, A. R. Hosseini, M. H. Wong, G. G. Malliaras, *ChemPhysChem* **2004**, *5*, 16.
[47] C. Chiang, S. Martin, J. Kanicki, Y. Ugai, T. Yukawa, S. Takeuchi, *Jpn. J. Appl. Phys.* **1998**, *37*, 5914.
[48] A. Cerdeira, M. Estrada, L. F. Marsal, J. Pallares, B. Iñiguez, *Microelectron. Reliab.* **2016**, *63*, 325.
[49] K. Fukuda, T. Someya, *Adv. Mater.* **2017**, *29*, 1602736.
[50] A. G. Polyravas, V. F. Curto, N. Schaefer, A. B. Calia, A. Guimera-Brunet, J. A. Garrido, G. G. Malliaras, *Flexible Printed Electron.* **2019**, *4*, 044003.